VIETNAM NATIONAL UNIVERSITY, HANOI
VIETNAM JAPAN UNIVERSITY

DO THI PHONG THU

SYNTHESIS OF HIGH-PERFORMANCE CATHODE MATERIAL $LiFePO_4$/C FOR Li-ION BATTERY

MASTER'S THESIS

VIETNAM NATIONAL UNIVERSITY, HANOI
VIETNAM JAPAN UNIVERSITY

DO THI PHONG THU

SYNTHESIS OF HIGH-PERFORMANCE CATHODE MATERIAL $LiFePO_4$/C FOR Li-ION BATTERY

MAJOR: NANOTECHNOLOGY

CODE: 8440140.11QTD

RESEARCH SUPERVISORS:

ASSOC. PROF. DR. NGUYEN XUAN VIET

PROF. DR. SC. NGUYEN HOANG LUONG

Hanoi, 2024

STATEMENT OF COMMITMENT

I acknowledge and fully understand the regulations against plagiarism. I pledge with my honor that the research presented herein is entirely my work and adheres to the Regulations on Prevention of Plagiarism in Academic and Scientific Research Activities at Vietnam Japan University, as outlined in Decision No. 700/QD-DHBVN dated 30/09/2021 by the Rector of Vietnam Japan University. This thesis is submitted as part of the requirements for the master's degree in Global Leadership. Any external sources utilized are duly acknowledged through explicit references.

Signature

ACKNOWLEDGEMENT

Firstly, I would like to express deep gratitude to Assoc. Professor Nguyen Xuan Viet and Professor Nguyen Hoang Luong who instructed me to do the research as well as helped me write this thesis.

I sincerely thank Mr. Dang Thanh Trong, Mr. Vu Quang Huy and all the members of the Electrochemical Laboratory, VNU University of Science, Hanoi. They helped and supported me in doing experiments and research. They are my good mentors and good friends who I'm very appreciated.

I would like to thank to all the lecturers in Vietnam Japan University, Hanoi who teach me useful lessons and knowledge. All the knowledge has been applied efficiently in doing this master thesis.

Finally, I want to thank my family that encourage and support me to complete this master thesis.

This research was funded by Vietnam Ministry of Science and Technology (MOET) under grant number ĐTĐL.CN 110/21 and by Vietnam Japan University, under the Research Grant Program of Japan International Cooperation Agency, code number of VJU.JICA.21.03

Student

Do Thi Phong Thu

TABLE OF CONTENTS

LIST OF FIGURES

LIST OF TABLES

LIST OF ABBREVIATIONS

CV: Cyclic voltammetry

XRD: X-ray diffraction

EIS: Electrochemical Impedance Spectroscopy

SEM: Scanning Electron Microscopy

LFP: Lithium iron phosphate

LFP/C: Lithium iron phosphate with carbon coating

NMP: N-methyl pyrrolidone

PVDF: Polyvinylidene fluoride

INTRODUCTION

From 1980s, the successful commercialization of Lithium-ion battery (LIB) has advanced the production of portable electronics such as laptops, mobile phones, cameras by the development of Information Technology (IT). This evolution led to a demand for rechargeable batteries with greater capacities, higher energy density, and a reduction in size and weight. Lead-acid, nickel-cadmium, and nickel-metal hydride batteries are some conventional rechargeable batteries which were available for development. They used aqueous electrolytes, which limit the increase of energy density and the reducing of size and weight. Therefore, there has been a crucial need for new, small, and lightweight batteries, which are to be put into practical usage. LIBs are one of the most advanced rechargeable batteries, attracting a lot of attention in recent years.

LIBs exhibit some excellent properties such as high capacity and energy density, low cost, and can operate at high current [1]. In LIBs, cathodes, anodes, and electrolyte all play significant roles in batteries performance. In particular, the cathodes material is considered to have the most impact in the operation of the cell. Cathode has the effect on the diffusion activity of Li^+ ion, which determines the capacity of the batteries.

There are several types of cathode material, like $LiCoO_2$, $LiMnO_2$, $LiFePO_4$. Among these materials, $LiFePO_4$ (LFP) shows several advantages compared to others. It is low-cost manufacturing, thermal stability, abundant in nature, and environmental friendliness. However, this material suffers from low conductivity and Li^+ diffusion rate, which hinders the performance of LIBs. Therefore, the are some methods to improve the properties of LFP, such as reducing particle size, doping and carbon coating.

There are several methods for synthesizing LFP cathode material, such as sol gel method, hydrothermal method, co-precipitation method and solid-state method. Co-precipitation method combined with solid state method is the popular choice because of its low cost, fast operation time and the result materials have uniform structure.

In this Master thesis, the objectives are:

Synthesize $LiFePO_4$/C Material:

- $FePO_4$ was synthesized using the co-precipitation method with a reflux process. The obtained $FePO_4$ was then utilized to synthesize $LiFePO_4$/C (LFP/C), with varying amounts of glucose used to prepare different LFP/C samples.

Investigate the Effects of Carbon Coating:

- The effect of carbon coating on the morphology and electrochemical properties of the material was investigated.

CHAPTER 1: OVERVIEW

1.1. Introduction of lithium-ion battery

1.1.1. Working principle of lithium-ion battery

LIB comprises of a cathode (positive electrode) and an anode (negative electrode), separated by an electrolyte containing lithium ions. These electrodes are isolated by a separator, typically a microporous polymer membrane, which allows the lithium ions to pass through but not the electrons. Additionally, polymer, gel, and ceramic electrolytes have been investigated for use in LIBs. Figure 1.1 illustrates the operational concept of a LIB. During charging, the battery is connected to an external electrical source. Electrons are released from the cathode and flow through the external circuit to the anode. Simultaneously, lithium ions move through the electrolyte from the cathode to the anode. The external electrical energy is converted and stored as chemical energy in the anode and cathode materials, which have different chemical potentials. In the discharging process, electrons flow in the diverse way, providing electrical power. Meanwhile, lithium ions move from the anode to the cathode through the electrolyte [2].

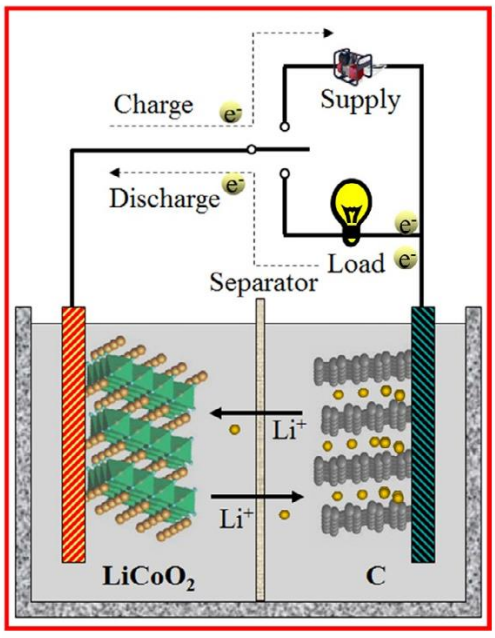

Figure 1.1. Working mechanism of a LIB [3]

Chemical energy is released from electrochemical reaction at the two electrodes [3]. The change of total Gibbs free energy by the reaction is determined by the electrodes. The theoretical cell voltage ($\Delta E = -\Delta G/nF$) can be calculated by charges transferred and overall electrochemical reaction.

1.1.2. Performances of lithium-ion battery

A number of parameters are used to investigate how well LIB can perform: specific energy, volumetric energy, specific capacity, cyclability, charge/discharge rate, safety, abuse tolerance. Specific energy (Wh/kg) measures the amount of energy per unit mass that the battery can store and release. The value is determined by multiplying the specific capacity, measured in ampere-hours per kilogram (Ah/kg), by the operating voltage, denoted in volts (V). Specific capacity quantifies how much charge can be stored per unit mass in a reversible manner, closely tied to the number of electrons involved in electrochemical reactions and the atomic weight of the material hosting the process. Cyclability, on the other hand, evaluates how effectively a lithium-ion battery can reverse its insertion and extraction processes over multiple charge and discharge cycles before significant energy loss or operational failure occurs. Several factors impact cycle life, including depth of discharge (DOD), state of charge (SOC), operating temperature, and battery chemistry. To extend cycle life, it's beneficial to limit DOD, minimize SOC fluctuations, and avoid high temperatures [2].

For LIBs, particularly in electric vehicles, having a high tolerance for abuse is crucial for practical use. Typically, prototypes undergo evaluations in mechanical, thermal, and electrical aspects to gauge their ability to withstand abuse. Thermal evaluations encompass tests for radiant heat, thermal stability, overheating, and extreme cold. Electrical evaluations include tests for short circuits, overcharging, over-discharging, and exposure to alternate currents. The significance of those abuse tolerance tests is paramount, especially in the context of electric vehicles, which are anticipated to rival conventional internal combustion engine-powered vehicles known for their resilience in harsh conditions.

The rate of charge or discharge, known as the C-rate, indicates how quickly a battery can be charged or discharged. At 1C, it is discharged or charged maximum energy in 1 hour, utilizing its maximum capacity within that time frame. For typical

LIBs used in personal electronics, such as mobile devices, it generally takes 1 to 4 hours to reach a full charge. LIBs used in electric vehicles may require longer charging times, sometimes overnight, although rapid charging to a certain low state of charge (SOC) is possible with specialized equipment capable of high currents. Improving rate performance is a significant focus in Li-ion battery research, aiming to reduce charging times notably [4, 2].

1.1.3. Components of lithium-ion battery

1.1.3.1. Anodes materials

The selection of anode materials is subject to extensive research, resulting in a wide range of potential candidates. The electrochemical properties of LIBs, such as their ability to withstand repeated cycles, charging speed, and energy storage capacity, are notably impacted by the choice of anode materials.

The initial LIBs used lithium metal as the anode because it has low molecular mass with high voltage, making it easy for electrons to transfer. However, the formation of lithium dendrites on the lithium metal anode surface during cycling led to short circuits, posing a substantial risk in LIBs [5]. Additionally, lithium metal is highly reactive to oxygen and moisture. Therefore, LIBs require to assemble in dry rooms or glove boxes to mitigate these risks.

Graphite is another dominant material for anode in LIBs nowadays. The layered structure of can enhance the movement of lithium ions within their lattice, minimizing irreversible reactions and thereby promoting excellent cyclability [6]. It has high theoretical capacity of 372 mA/g.

Other elements and compounds are also investigated as materials for anode. Element like silicon (Si) [7] and compound like metal oxides [8] show promise as the alternative to carbon. Si has an excellent theoretical capacity (4200mAh/g). easily to alloy and de-alloy with lithium. Although metal oxides have low conductivity, they still exhibit promising properties in Li^+ diffusion activity.

1.1.3.2. Cathode materials

Several types of material have been investigated for synthesize cathode for lithium-ion batteries, categorized by the voltage and versus lithium and crystal structure. Figure 1.2 shows the 3 main lattice structures of cathode materials for LIBs. These are layered, spinel and olivine structures.

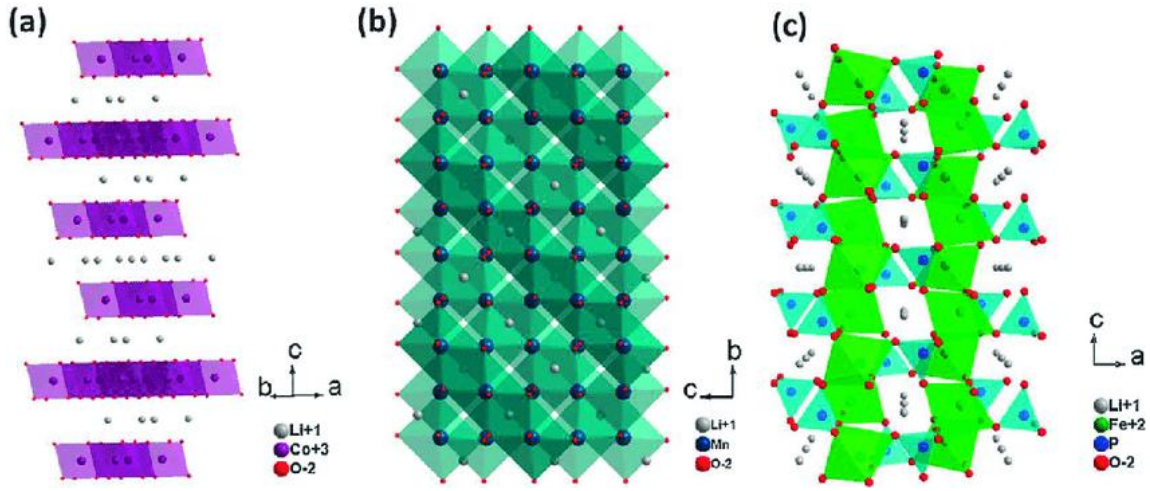

Figure 1.2. Structure of cathode material for lithium battery a) layered, b) spinel and c) olivine [9]

Table 1.1 presents the cathode materials of each structure. Transition metals are the popular choice for cathode synthesis. $LiCoO_2$ with layered structure is the most used in commercial LIBs. It has a theoretical capacity of 274 mAh/g, good cycle life (500 cycles). $LiCoO_2$ is readily scalable for large scale manufacturing and exhibits stability in ambient air conditions. However, it has several disadvantages such as high material cost, toxicity of cobalt, and unstable at high temperature [1].

Table 1.1. Cathode materials with different crystal structure [10]

Crystal structure	Compound
Layered structure	LCO $LiCoO_2$
	NMC $LiMO_2$ (M= Ni, Co, Mn) NCA $LiMO_2$ (M=Ni, Co, Al)
Spinel structure	LMO $LiMnO_2$
Olivine structure	LFP $LiFePO_4$

Polyanion material types such as PO_4, SO_4, SiO_4 are attracted a lot of attention due to its low cost and low impact on environment. Among the materials, $LiFePO_4$ offers several advantages, that are thermal stability, long cycle life, and environmental friendliness. However, $LiFePO_4$ has some disadvantages of poor electronic and ionic conductivity and low capacity [11].

1.1.3.3. Binder

The performance of the electrode in LIB is influenced by the choice of binders. Typically, the active material, additive carbon particles, and binder are combined to form anode or cathode, with the binder content of 4-15 % of the mixture. Polyvinylidene fluoride (PVDF), a thermoplastic polymer, is commonly used as a binder for both cathode and anode materials [13].

To tackle this challenge, binders containing carboxylic groups like carboxymethyl cellulose (CMC), poly acrylic acid (PAA), and alginate are used. These polymers possess properties that promote the formation of a stable solid electrolyte interface (SEI) layer and can accommodate volume changes in active particles [14].

1.1.3.4. Electrolyte

The electrolyte components and properties have a considerable effect on the capacity and cycling performance of LIBs. The selection of electrolyte is critical to endure the redox environment on both cathode and anode sides, as well as the voltage range, avoiding experiencing decomposition or degradation. Moreover, the electrolyte needs to be inert and have good stability in wide temperature range. For the commercial LIBs, the liquid electrolyte consists of lithium salts dissolved in organic solvents.

However, the organic solvent can easily catch fires due to thermal runaway or short circuit. Therefore, electrolyte needs to have low flammability, and to be environmentally friendly and cost-effective to produce. Some kinds of solvent, like carbonate solvents characterized by high dielectric constants, are chosen to effectively dissolve lithium salts at high concentration, typically around 1 M. The viscosity and melting point of the solvent should be low in order to ensure high ionic mobility within the operating temperature range. A variety of lithium salts have been investigated, such as $LiPF_6$, $LiBF_4$, $LiClO_4$, and $LiCF_3SO_3$. It is important to note that the selection of anions aims to avoid their oxidation on the charged surface of the cathode. Among the salts, $LiPF_6$ stands out due to its favorable combination of safety, conductivity, and good ion mobility. However, it is crucial to handle $LiPF_6$ electrolyte with care because it reacts with H_2O to form HF, which is a very corrosive compound. Therefore, minimizing moisture is essential when handling this electrolyte [2].

1.1.3.5. Separators

The separator plays a crucial role in preventing short circuits by obstructing electron flow between the cathode and anode while facilitating the passage of lithium ions. It must exhibit thermal, chemical, and electrochemical stability towards the electrolyte, possess porous structures, and be robust to withstand high currents [15].

Commercial LIBs commonly employ polypropylene (PP) and polyethylene (PE) films as separators. PP and PE are favored for their ability to maintain battery performance over long cycles. However, PP may lack the necessary width to effectively prevent short circuits, potentially leading to battery malfunction. Consequently, PE is preferred over PP because it shows its superior ability to prevent short circuits and ensure battery integrity [15].

1.2. Introduction of $LiFePO_4$ cathode material

1.2.1. Structure and properties of the material

1.2.1.1. Structure of $LiFePO_4$ material

$LiFePO_4$ (LFP) has a structure belonging to the olivine type material. Figure 3.1 shows the crystal structure of LFP. It has the orthorhombic structure, with the unit cell volume of 0.392392 nm^3, and the lattice parameters are a = 0.6008 nm, b = 1.0334 nm,

and c = 0.4693 nm. The oxygen atoms are arranged in a hexagonal close packing arrangement. Phosphorous (P) atoms are at the tetrahedral position to form tetrahedron PO_4. Iron (Fe) ions arrange themselves into zigzag chains of octahedrons within alternate basal planes. The chains in the structure are linked together by PO_4 groups Meanwhile, lithium (Li) atoms are situated in octahedral sites located in the remaining basal planes. These Li^+ ions form one-dimensional tunnels within the material's structure, running parallel to the planes formed by FeO_6 octahedra that share corners. Specifically, these tunnels extend along the [010] direction within the orthorhombic Pmnb lattice [16].

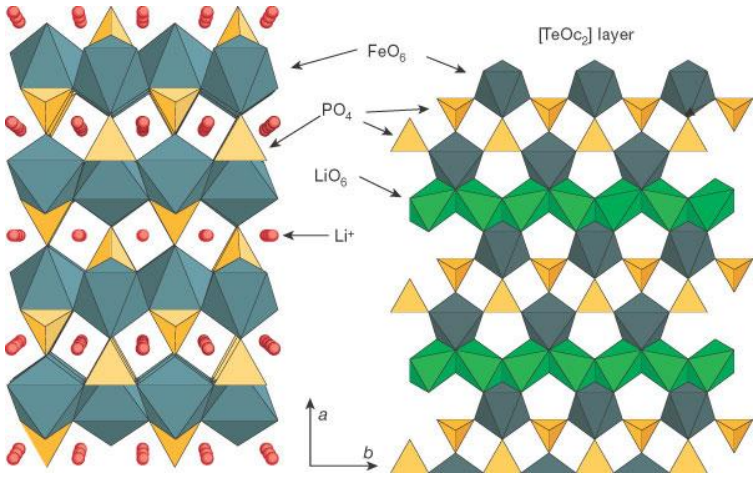

Figure 1.3. Crystal structure of LiFePO4 material [17]

1.2.1.2. Properties of $LiFePO_4$ material

The strong covalent bonds between oxygen and P^{5+} ions play a crucial role in stabilizing the structure of LFP. This stability is notably different from layered oxides, where the oxide layers are less tightly bound [18]. The strong covalent interactions also stabilize the Fe^{3+}/Fe^{2+} antibonding state through an inductive Fe–O–P effect. Consequently, oxygen atoms within the structure become more resistant to extraction [18]. These characteristics ensure stable operation even at elevated temperatures and enhance safety under harsh conditions, making LFP highly attractive for a wide range of applications [19]. Excellent cycling reversibility is achieved because $LiFePO_4$ and $FePO_4$ share an isostructural configuration (space group Pnma), differing only slightly in cell parameters. Specifically, when $LiFePO_4$ undergoes delithiation to form $FePO_4$, the volume decreases by 6.81%, and the density increases by 2.59% [20]. Furthermore,

the structure contains vacant interstitial sites that offer Li^+ ions greater mobility. Electrochemical studies have demonstrated the reversible insertion and extraction of Li^+ ions into and from these interstitial sites [21].

However, it's important to acknowledge three inherent drawbacks of LFP for LIBs: Firstly, the significantly low electronic conductivity, with conductivity below 10^{-9} S/cm, hinders the full utilization of its theoretical capacity [22]. The poor conductivity is likely attributed to the corner-sharing linkage of FeO_6 rather than edge- or face-sharing, along with the substantial separation between Fe atoms [23]. Furthermore, olivine-type materials exhibit lower true volumetric density compared to other lithium-ion battery materials, with $LiMnPO_4$ at 3.4 g/cm^3, $LiFePO_4$ at 3.6 g/cm^3, $LiMn_2O_4$ at 4.2 g/cm^3, $LiNiO_2$ at 4.8 g/cm^3, and $LiCoO_2$ at 5.1 g/cm^3 [20, 24]. Moreover, they also possess a low Li-ion diffusion rate, from 10^{-11} to 10^{-13} cm^2 s^{-1} [25].

1.2.2. Li^+ diffusion process for LFP material

Lithium intercalation and de-intercalation involve a two-phase reaction, resulting in $LiFePO_4$ and $FePO_4$ as end members. Both materials have the same structure, and within $LiFePO_4$, lithium ions can only migrate along the [010] direction (b-axis) due to the absence of continuous LiO_6 octahedra along the a and c axes [26]. Islam et al [27] using first principle to calculate that the one-dimensional diffusion channel with the lowest activation energy path occurs along the [010] direction, indicating higher mobility compared to other transport channels with higher energy barriers. In contrast to other cathode materials, for example, layered cathodes with two-dimensional Li-ion diffusion and spinel-structured cathodes like $LiMn_2O_4$ (e.g., $LiNi_{0.5}Mn_{1.5}O_4$) featuring three-dimensional Li-ion diffusion channels, olivine LFP exhibits one-dimensional diffusion [28, 29]. Therefore, the diffusion of lithium ions in LFP is not only limited but also susceptible to defects [30, 31].

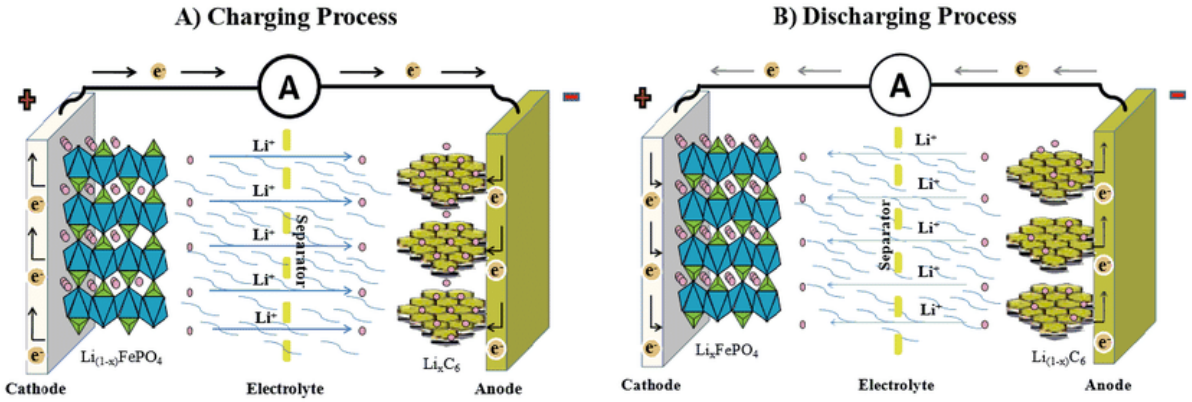

Figure 1.4. Charging and discharging process of LFP cathode material [32]

The charging and discharging process of LIB with LFP as cathode material is shown in figure 1.4. During electrochemical reactions, both lithium ions and electrons migrate in specific paths. In the case of $LiFePO_4$, during the charging process, lithium ions de-intercalate from the $LiFePO_4$ crystal and move toward the anode through the electrolyte. Concurrently, electrons also move from $LiFePO_4$ to maintain electrical neutrality as Lithium-ions are exported (the discharge process is reversed). The duration of lithium ions de-intercalating from a $LiFePO_4$ crystal is primarily influenced by diffusion dimensions, path accessibility, and the length of lithium ions within the $LiFePO_4$ (or $FePO_4$) crystal. If the duration is prolonged due to limited diffusion dimensionalities or obstructed pathways, lithium ions will not diffuse efficiently, leading to concentration polarization. Similarly, if conductivity is inadequate, meaning electrons cannot transfer efficiently to sustain electrode reactions, electrochemical polarization occurs [33].

In studying the intrinsic kinetics of Li^+ insertion/extraction within LFP electrodes during charge/discharge processes, it is essential to examine the diffusion of Li^+. It's established that Lithium-ion diffusion in LFP is a one-dimensional phenomenon along the b-axis. Various models describe Li^+ intercalation/de-intercalation in LFP, including the shrinking-core [34], mosaic [35], core-shell [36], and domino-cascade models [37]. In the shrinking-core model proposed by Srinivasan and Newman [34], , lithium de-intercalation occurs from the surface of the particle towards the center. In contrast, Laffont et al. [35] utilized high-resolution transmission electron microscopy coupled with electron energy loss spectroscopy to demonstrate that $FePO_4$ remains in the core of

the particle while LFP forms the shell of chemically delithiated nanosized particles, establishing the core-shell model. Delmas et al. [36] developed the domino-cascade model, which proposes a single-phase existence at the particle level and a two-phase distribution at the electrode scale, illustrating the influence of collective effects during electrochemical delithiation.

1.2.3. Methods for synthesizing of LiFePO4 material

1.2.3.1. Hydrothermal method

$LiFePO_4$ nanoplates with the thickness 20 nm and 50 nm width were synthesized by hydrothermal method. The mixture of $FeSO_4.7H_2O$, H_3PO4, LiOH, ascorbic acid, $C_{18}H_{29}SO_3Na$ (SDBS) with the ratio 3:1:1:0.5:0.2 in 40 ml distilled water were transferred into 50 ml Teflon stainless steel, it was heated at 170 ℃ in 24h [38].

1.2.3.2. Sol-gel method

Porous micro-spherical $LiFePO_4$ composites were prepared by sol-gel method. The mixture of Li_2CO_3, $Fe(NO_3)_3.9H_2O$, H_3PO_4, and tartaric acid were mixed in water to form a gel. The gel was heated at 120℃ for 48h, and sintered at 700℃ for 12h in argon atmosphere [39].

Nanosized $LiFePO_4$/C particles were synthesized by citric acid as chelating agent and carbon source [40].

1.2.3.3. Co-precipitation method

LiOH solution was added to the solution of $(NH_4)_2Fe(SO4)_2.6H_2O$ and $NH_4H_2PO_4$ with blowing nitrogen gas to the solution. The obtain green precipitates were obtained, then heated to 120 ℃ for 5 h and sintered at 700 ℃ for 18h under argon flow [41].

Slowly mixing solutions of $Fe(NO_3)_3$ and $(NH_4)_2HPO_4$, both at 0.1 mol L^{-1} in a stoichiometric ratio, followed by stirring for an hour, produced a pale yellow precipitate upon dropwise addition of concentrated NH_3 solution to adjust the pH between 2 and 5, maintaining a temperature of 60°C to prevent $Fe(OH)_3$ formation. After stirring the precipitates with the mother liquor for 30 minutes, they were collected via filtration,

washed with deionized water several times, and dried under vacuum at 100°C for 4 h. The obtained $FePO_4.H_2O$ samples were then heated at 600 ℃ and keep sintering in air for 4 h to obtain $FePO_4$. The synthesized $FePO_4$ materials were mixed with Li_2CO_3 and glucose by ball milling. The mixture was annealed at 720 ℃ for 12h in nitrogen flow to obtain $LiFePO_4$/C [42].

In this research, LFP was synthesized from co-precipitation method because the synthesis process is simple and large amount of material can be produced, which can apply to mass-production.

1.2.4. Methods for improving the performance of $LiFePO_4$ material

LFP is widely used commercially, but its application is restricted by its relatively low capacity compared to other cathode materials. The goal is to understand how to reach and surpass the theoretical capacity of 170 mAh/g. There are several methods for improving the performance of LFP.

1.2.4.1. Reducing particle size

By controlling the morphology and particle size of lithium iron phosphate (LFP), its crystal structure can be altered to shorten pathways for lithium-ion diffusion and optimize well-oriented facets. This modification proves highly effective in enhancing the rate capacity of LFP. Reducing LFP particles to the nanoscale enables high-power density, primarily attributed to the shortened pathways for Li^+ diffusion within the 1D channel of LFP. The fabrication of well-oriented nanometric phospholivine LFP typically involves low-temperature processes, such as solvothermal, hydrothermal, and co-precipitation methods, as opposed to conventional dry synthesis (solid-state) methods [43]. Precisely controlling synthesis parameters such as reactant concentration, sources, reaction time, temperature, pH, and procedure is crucial for influencing the morphology, defect chemistry, and properties of lithium iron phosphate (LFP) [44]. However, reducing particle size to the nanoscale can diminish volumetric energy density due to increased surface area, necessitating more binders and causing undesirable reactions, ultimately resulting in poor cycling life. To address these limitations, the fabrication of micro-nanostructure materials emerges as a viable approach for enhancing LFP performance. This approach leverages both nanoparticles and micro-sized

structures, capitalizing on the advantages of each. LFP nanoparticles facilitate high-rate performance by shortening Li^+ diffusion pathways, while micro-sized structures offer the benefits of both high volumetric energy density and cycling performance [45]. Porous micro-nano structured, starfish-like LFP/C composites were synthesized by solvothermal method, reported by Chen et al. It exhibited high-rate capabilities (157.5, 113.7, 86.7 mAh/g at 1 C, 10 C, and 20 C) and excellent cycling stability (98.4% after 100 cycles at 1 C) [46].

1.2.4.2. Carbon-coating

The aim of using carbon for coating is to enhance electron movement and surface conductivity. This facilitates the utilization of the active material at high rates [47]. Improvement of electrical conductivity and surface degradation prevention can be observed when carbon is coated. Furthermore, incorporating carbon into the LFP cathode material functions as a nucleating agent, restraining the expansion of LFP grains. This restriction leads to improved ionic conductivity by reducing the diffusion distance for Li^+ ions. In addition, the oxidation of Fe^{2+} can be prevented because the carbon layer act as reducing agent [48, 49].

The carbon coating process follows using various precursors serving as carbon source, then mix with cathode material, and heat at high temperature in noble gas environment. There are some factors affecting the performance of LFP/C: (1) thickness, (2) degree of graphitization, and (3) the coating layer structure. If the carbon layer is too thick, the diffusion of Li^+ will decrease and the capacity and energy density dramatically drop. For too thin carbon layer, it does not cover the cathode material uniformly, leading to the decrease of capacity and energy density. The precursors for the carbon source comprise of organic substances (glucose, sucrose, lactose, citric acid) and inorganic substances (graphene, super P, carbon nanotubes). Typically, organic compounds present the benefit of forming a consistent coating layer structure, ensuring uniformity in thickness and coverage on LFP. Moreover, these compounds can readily convert into carbon during pyrolysis. However, regulating the quality of carbon, including its conductivity and graphitization level, proves challenging. Conversely, inorganic carbon sources offer contrasting advantages and drawbacks [50, 51].

1.2.4.3. Doping

Doping is another way to improve the performance of LFP besides size control and carbon coating. The addition of ions that replace the small amount of Li^{+}, Fe^{2+}, O^{2-} sites will increase the conductivity, diffusion rate, and performance of charge/discharge at high current rate. Doping includes single element doping and multielement doping. For single element doping, ions can be doped at Li site, Fe site or O site. In Li site, ions with small ionic radius such as Na, K, Al, Nb. The width of diffusion path of Li-ions can be increased, and the resistance of charge transfer will be decreased. Nb-doped LFP exhibited higher conductivity than undoped LFP (about 10^{6} at room temperature. For Fe sites, alkali ions are the major use. Mg-doped LFP enhances the electronic and ionic transport of the material. The conductivity when doping at O site is much higher than doping at Fe site. Anion/O-site doping has a unique impact on the lattice parameters of LFP, particularly altering the parameters a and b while leaving the parameter c unchanged, a phenomenon not observed with cation doping. Anion-doped LFP has been shown to exhibit significantly improved high-rate performance and cycling stability. Okada et al. demonstrated this by producing sulfur-doped LFP nanoparticles with a diameter of approximately 100 nm using thioacetamide as a sulfur source via the solvothermal method. Due to sulfur's larger ionic radius compared to oxygen, the lattice parameters a and b expanded by 0.2%, while there was only a negligible increase in c (0.03%) [52].

In this research, the performance of the LFP material was improved by carbon coating method, using glucose as the carbon source. This method is low cost and the synthesis process is simple.

CHAPTER 2: EXPERIMENTAL

2.1. Chemicals and apparatus

2.1.1. Chemicals

The chemicals used are listed in table 2.1

Table 2.1. List of chemicals used

Name	Chemical formula	Manufacturer
Iron (II) sulfate heptahydrate	$FeSO_4.7H_2O$	Xilong, China
Mono ammonium phosphate	$NH_4H_2PO_4$	Duc Giang Group, Vietnam
Acid sulfuric	H_2SO_4	Duc Giang Group, Vietnam
Hydrogen peroxide	H_2O_2	Duc Giang Group, Vietnam
Glucose	$C_6H_{12}O_6$	China
Lithium carbonate	Li_2CO_3	China
Polyvinylidene fluoride (PVDF)	$(CH_2CF_2)n$	China
N-Methyl-2-pyrrolidone (NMP)	C_5H_9NO	China
Lithium metal	Li	China
Aluminum foil	Al	China
Carbon black	C	China
Lithium hexafluorophosphate	$LiPF_6$	Sigma Aldrich
Ethylene carbonate	$(CH_2O)_2CO$	Sigma Aldrich
Dimethyl carbonate	$OC(OCH_3)_2$	Sigma Aldrich

2.1.2. Apparatus

- Analytical balance (Japan)

- Furnace (China)

- Argon-fill glove box (USA)

- Vacuum oven (Germany) and some other instruments

2.2. The synthesis of $LiFePO_4/C$

The synthesis of $LiFePO_4/C$ (LFP/C) composites were followed by 4 steps:

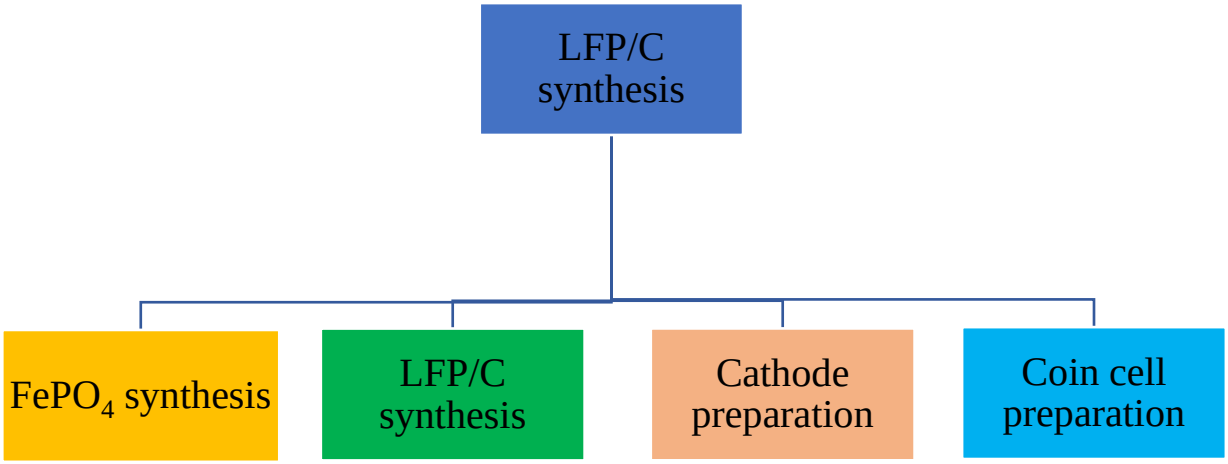

Figure 2.1. Experimental procedure in the synthesis of LFP/C

2.2.1. Synthesis of $FePO_4$

$FePO_4$ powders were synthesized from precipitation method by reflux process, using $FeSO_4.7H_2O$ and $NH_4H_2PO_4$ (MAP) as precursors. 27 g $FeSO_4.7H_2O$ (0.1 mol) was dissolved in 170 ml distilled water. 1.62 ml of H_2SO_4 was slowly added to the solution to prevent the hydrolysis of Fe^{3+}. Next, 7.5 ml of H_2O_2 was slowly added to the solution. The mixture was heated to 90 ℃. 11.5 g of MAP (0.1 mol) was dissolved in 170 ml H_2O, heated to 90 ℃. Then, MAP solution was poured into $FeSO_4.7H_2O$ solution, the temperature was kept at 90 ℃, and refluxed in 2 hours. After the reaction, the white precipitate of $FePO_4.H_2O$ was obtained, filtered, washed several times with

distilled water and dried at 80 ℃ in vacuum. The obtained powders were sintered at 550 ℃ in 5 hours.

Figure 2.2. Experimental procedure for synthesizing $FePO_4$

2.2.2. Synthesis of LFP/C

The synthesized FePO4 powders were mixed with Li_2CO_3 powder, the ratio of $FePO_4$:Li_2CO_3 was 2:1. Different amounts of glucose were added as the reducing agent and carbon source. Distilled water was used as solvent. The mixture was ball-milled with the speed 200 rpm in 6 hours. After mixing, the mixture was dried in vacuum at room temperature. After drying, the mixture was sintered at two temperatures: 350 ℃ in 5 hours and then 700 ℃ in 12 hours in Argon atmosphere. After sintering, $LiFePO_4$ with carbon coating was obtained.

Table 2.2. Glucose content in each sample

Sample	Glucose mass content (%)
LFP/C-G15	15 %
LFP/C-G20	20 %
LFP/C-G25	25 %

Figure 2.3. Experimental procedure for synthesizing LFP/C

2.2.3. Cathode preparation

LFP/C samples were mixed with carbon black and PVDF with the ratio 0.9:0.05:0.05 respectively in NMP solvent and stirred for 2 hours to form slurry. After that, the slurry was casted on Al foil, and then dried at 120℃ for 10h in vacuum. The electrode was cut into circular strips with diameter of 13 mm and mass density of 3-4 mg/cm^2.

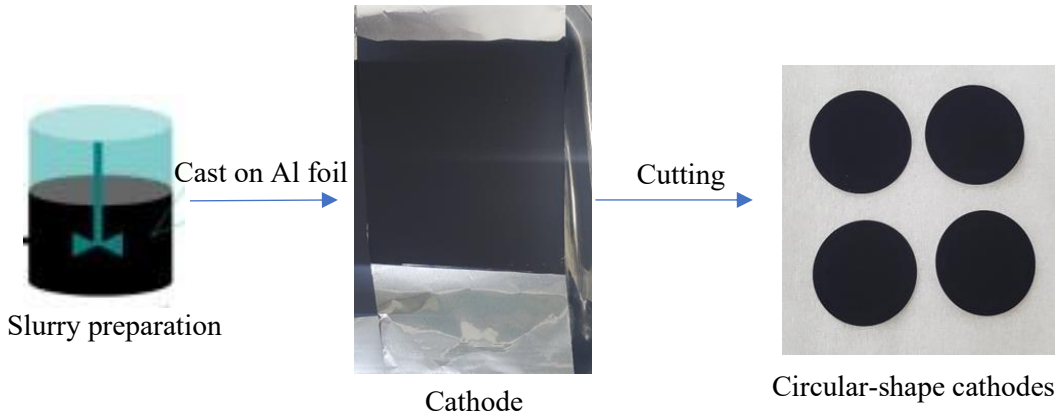

Figure 2.4. Experiment procedure for cathode preparation

2.2.4. Coin cell preparation

Coin cell was prepared in an argon-filled globe box with $LiFePO_4$/C as cathode, a Li foil as an anode, a 1M $LiPF_6$ solution ethylene carbonate-dimethyl carbonate (1:1 v/v) as an electrolyte, and a porous polypropylene film as a separator.

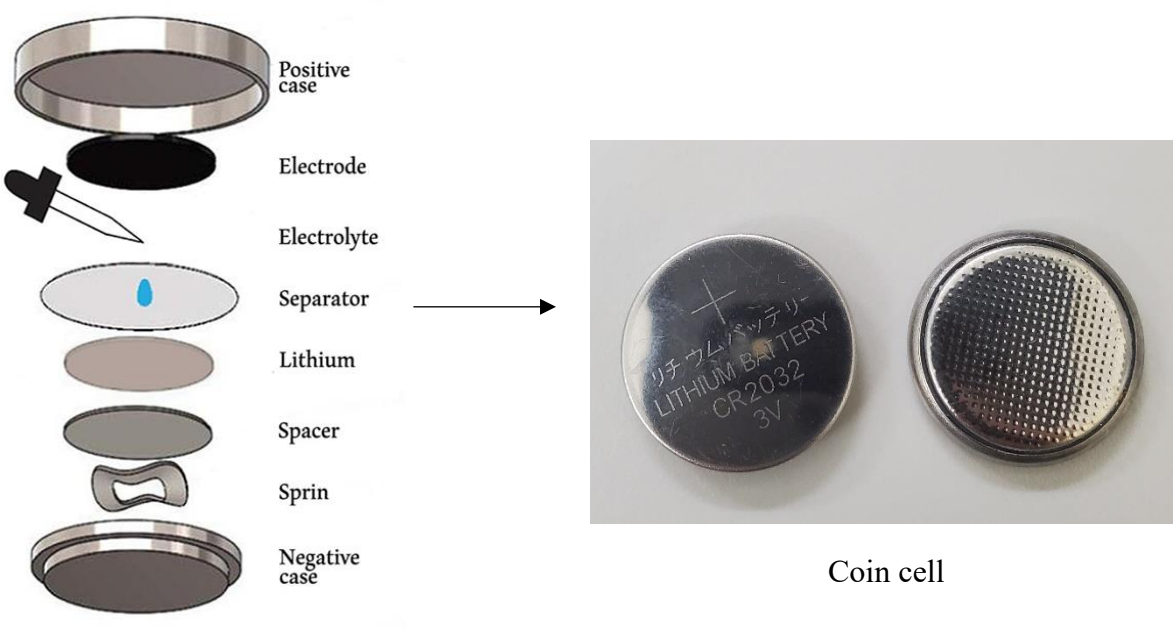

Coin cell components

Coin cell

Figure 2.5. Coin cell preparation

Figure 2.6. Argon-fill Glove box

2.3. Characterization methods

2.3.1. Scanning Electron Microscopy (SEM)

A Scanning Electron Microscope (SEM) is a type of electron microscope that can generate high-resolution images (from tens to hundreds of thousands of times) of the surface of a specimen by using a narrow electron beam scanning over the sample surface. Image formation of the specimen is achieved by detecting and analyzing the radiation emitted from the interaction of the electron beam with the specimen surface. The SEM is used to study surface morphology and the structure of thin layers beneath the surface, as well as to investigate electrode surfaces or corroded surfaces. It is also employed for chemical analysis of surface composition.

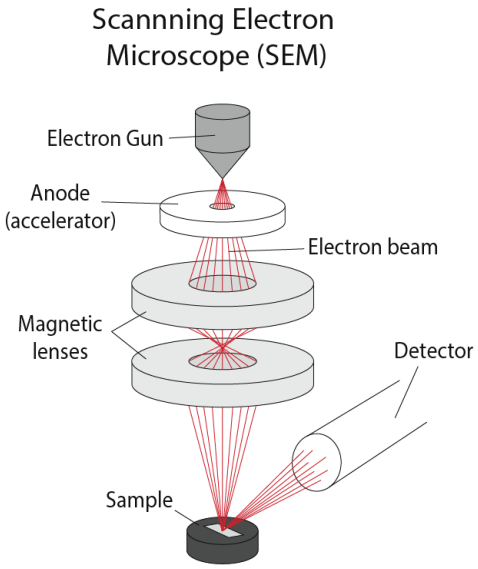

Figure 2.7. SEM operation principle

The principle involves using an electron beam generated at an electron source, accelerated in an electric field, and then converted into a narrow electron beam ranging from a few angstroms to several nanometers in size through a system of converging lenses. Subsequently, the electron beam scans over the surface of the sample using static electromagnetic coils to capture the morphological image of the entire sample surface. One or multiple detectors collect secondary electrons reflected from the sample, synchronized with the signals received from the detector after amplification is projected onto a fluorescent screen to produce an image of the sample's structure.

2.3.2. X-ray diffraction (XRD)

The basis of X-ray diffraction method relies on the phenomenon of X-ray scattering by the crystal lattice. When X-rays interact with matter, they cause elastic scattering with electrons of atoms within the material's crystalline structure, resulting in X-ray diffraction phenomena. According to the theory of crystal structure, the crystal lattice is constructed from atoms or ions distributed evenly in space in a specific orderly manner. When an X-ray beam reaches the surface of a crystal and penetrates into its lattice, this lattice acts as a unique scattering medium. The atoms or ions stimulated by the X-ray beam emit reflected rays. Additionally, these atoms or ions are distributed on parallel planes.

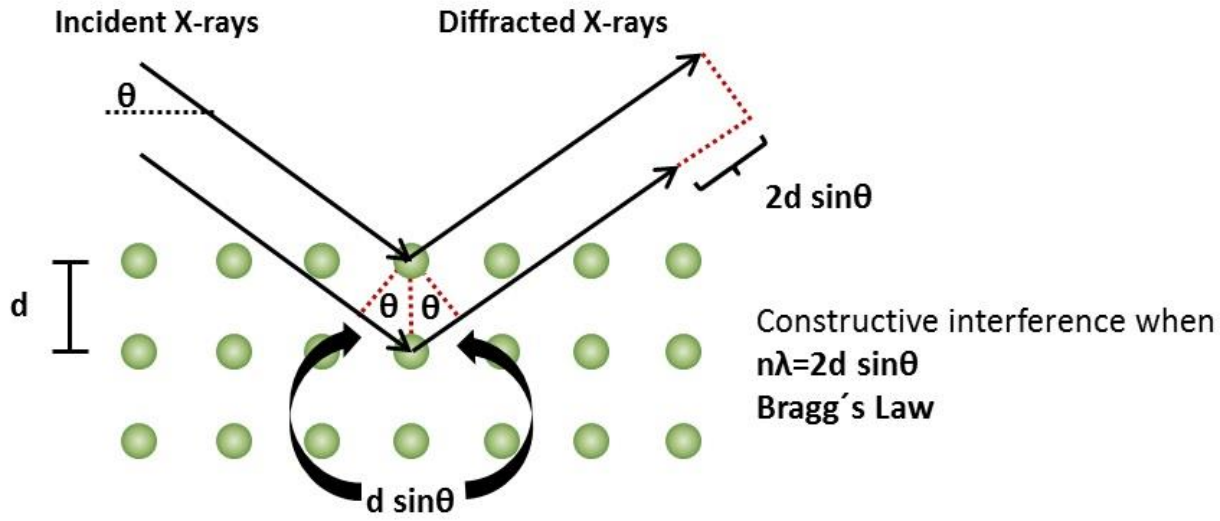

Figure 2.8. X-ray diffraction principle

The relationship between the distance of two diffraction planes (dhkl), the angle between the X-ray beam and the reflecting plane (θ), and the wavelength (λ) is expressed by the Bragg's law equation:

$$2d_{hkl}\sin\theta = n\lambda \qquad (1)$$

Here, λ represents the wavelength of the X-ray, θ denotes the angle between the X-ray beam and the reflecting plane, d is the distance between two consecutive crystal planes, and n is the order of diffraction. This equation describes the conditions under which X-rays are diffracted by the crystal lattice, allowing scientists to determine

structural information about the crystal, such as interplanar distances and atomic arrangements.

From the conditions of diffraction, it is evident that each type of crystal with a specific lattice structure will produce diffraction patterns with defined positions, intensities, and quantities of diffraction spots, characteristic of that lattice type. Therefore, the crystal structure of the studied material can be determined through X-ray diffraction patterns.

2.3.3. Cyclic voltammetry

Cyclic Voltammetry (CV), also known as the von-Ampe method, is used to determine the diffusion coefficient (D) and investigate the reversible variation (rechargeability) of the studied material. CV is an electrochemical method that measures the current generated in an electrochemical cell under conditions where the applied voltage exceeds the limit defined by the Nernst equation. CV is performed by cyclically varying the potential of a working electrode and measuring the resulting current.

In this measurement method, the electrode surface must be pre-restored before measurement, the solution should not be stirred, and mass transport occurs via diffusion. The polarization curve is a cyclic curve representing the relationship between current density (I) and potential (E). The shape of the cyclic voltammogram depends on solvent selection, supporting electrolyte, and electrode nature. The scan rate is typically limited to between 1 mV/s and 1000 mV/s. It should not be lower than 1 mV/s to avoid convection stirring of the diffusion layer.

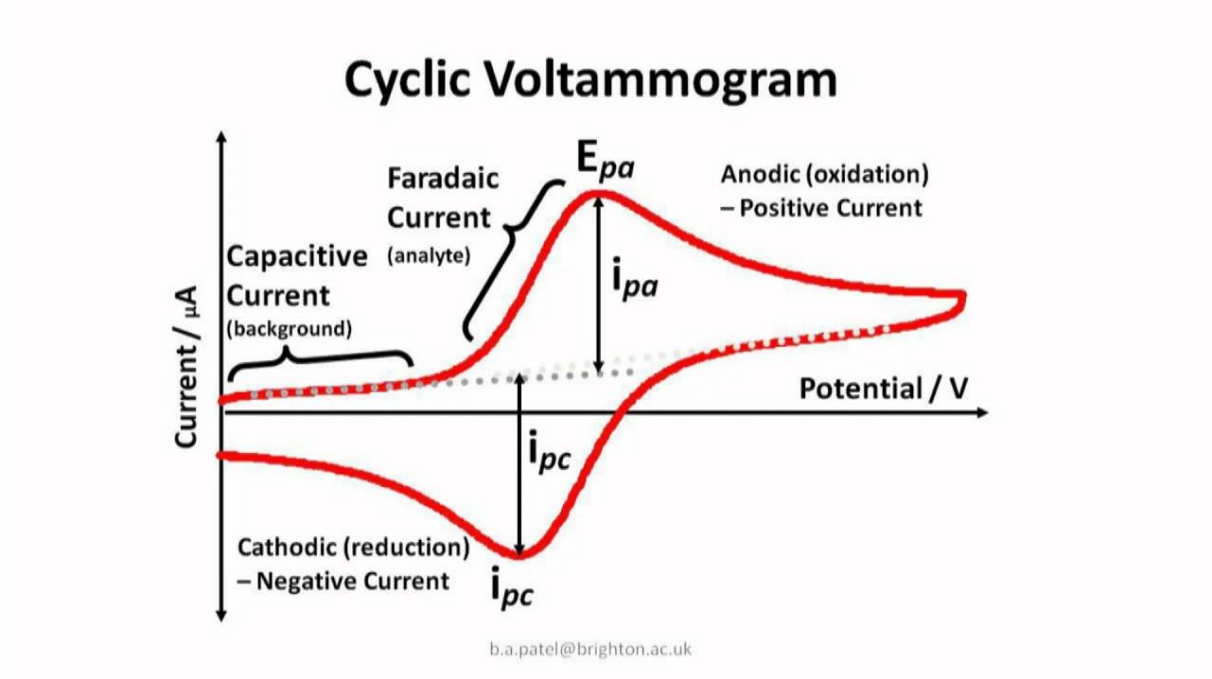

Figure 2.9. Cyclic Voltammetry curve

The cyclic voltammogram, which represents the relationship between current (I) and potential (E), is a curve that exhibits a characteristic peak (I_p) where the maximum current (I_p) corresponds to the peak potential (E_p). For reversible redox processes of the type Ox + ne- ⇌ Red, which are diffusion-controlled, Randles-Sevcik derived a relationship between the peak current and the scan rate:

$$I_p = 2.687 \times 10^5 \times n^{3/2} A D_o^{1/2} C_o v^{1/2} \quad (2)$$

Here:

- n: number of electrons involved in the reaction
- v: scan rate (V/s)
- A: electrode area (cm^2)
- C_0: concentration of the reacting substance (mol/cm^3)
- D_o: diffusion coefficient (cm^2/s)

The anodic peak potential (E_{pa}) and cathodic peak potential (E_{pc}) for the reversible redox process are described by the equation:

$$E = E_{pa} - E_{pc} = 0.059/n \quad (3)$$

These are fundamental in cyclic voltammetry for analyzing electrochemical reactions, determining diffusion coefficients, and understanding the kinetics of redox processes.

In this measurement method, one can use a single scan (one cycle) or perform multiple successive cycles (multiple sweeps). In the case of multiple cycles, the i-E curves are continuously scanned, where the applied potential is cyclically varied over time. During the cyclic voltammetry scan, based on the obtained curves and other data, it is possible to determine the number of reactions occurring or the stages of the reaction, depending on the appearance of peaks, break points, or inflection points on the graph. If peaks are not well-defined or clear, or if they are ambiguous, it could indicate the presence of side reactions.

2.3.4. Electrochemical impedance spectroscopy

The principle of electrochemical impedance spectroscopy (EIS): When a small sinusoidal oscillation with amplitude sin U_0, and angular frequency $\omega = \pi\ 2f$ is applied through an AC generator, a corresponding sinusoidal current with amplitude I_0 and frequency ω will be generated, but phase-shifted by an angle φ relative to the applied voltage, will appear in the circuit.

According to Ohm's law, impedance Z can be defined as:

$$Z = u / I = f(\omega) \quad (4)$$

$Z(\omega)$ is a complex function, $Z(\omega) = Z_{re} + jZ_{im}$

- Z_{re} is the real part of impedance (resistance component),
- Z_{im} is the imaginary part of impedance (reactance component),
- j is the imaginary unit ($j = -1j$)

The equivalent circuit diagram of an electrochemical cell is represented as follows:

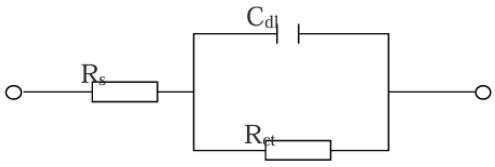

Figure 2.10. Circuit diagram

R_s: Solution resistance.

R_{ct}: Charge transfer resistance, which includes the resistance of the electrode and the surface processes.

C_{dl}: Double layer capacitance, representing the capacitance due to the accumulation of charges at the electrode-electrolyte interface.

In the graph, the relationship between $-Z_i$ and Z_r will result in a semicircle with a radius equal to $(R_{ct} - R_s)/2$. R_{ct} and R_s can be determined at the intersection point of this semicircle with the Zr axis. The double-layer capacitance C_{dl} can be determined from R_{ct} and the value of the frequency fmax at which the imaginary impedance Zi reaches its maximum.

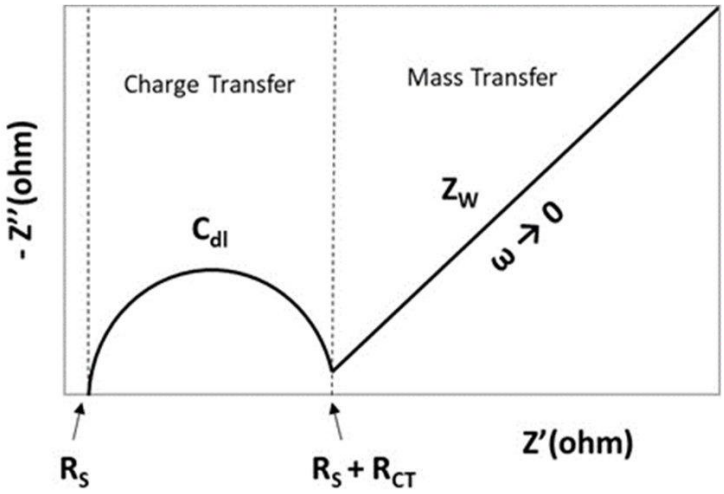

Figure 2.11. EIS curve

2.3.5. Charge-discharge measurement

Charge- discharge measurement is used to investigate some factors of Li ion battery such as specific energy, specific capacity, cycling ability of Li-ion batteries. For the charging process, constant current is applied, and the voltage of the cell will rise. The voltage will reach the cut off voltage when the battery is fully charged, then the capacity of the cell can be measured. In the discharging process, the voltage drops due to the battery releasing energy, and the amount of capacity that it can release can be measured. The measurement of how many times the battery can charge and discharge is very important to investigate the cycle life of a battery.

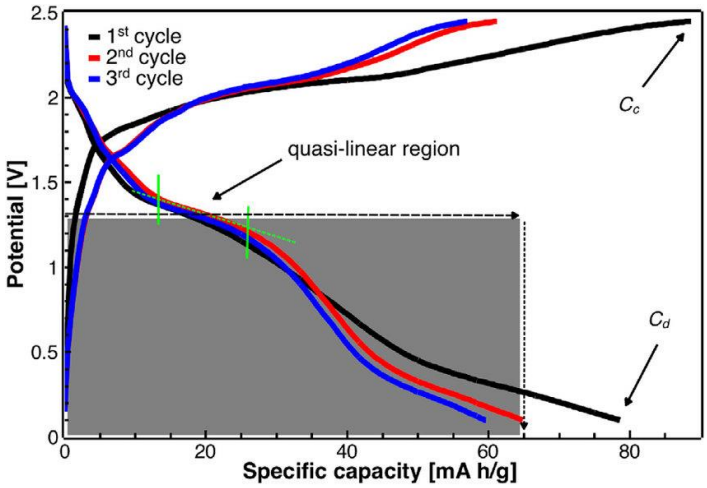

Figure 2.12. EIS curve

The charge discharge rate can be changed by changing the C-rate. C rate is the value of current that the battery charge or discharge at. Typically, 1C rate represents the capacity that a battery can charge or discharge in 1 hour. For example, a battery with capacity 5Ah can be provide 5 A in 1 hour. That 5 Ah battery is discharged at 0.5C will release 5 A in 2 hours. And if at 2C, it will give 10 A in 30 minutes. The C-rate investigation is very important in the manufacturing of batteries for high energy systems or devices.

CHAPTER 3: RESULTS AND DISCUSSION

3.1. Structure and morphology of $FePO_4$ and LFP/C samples

3.1.1. Morphology of $FePO_4$ and LFP/C samples

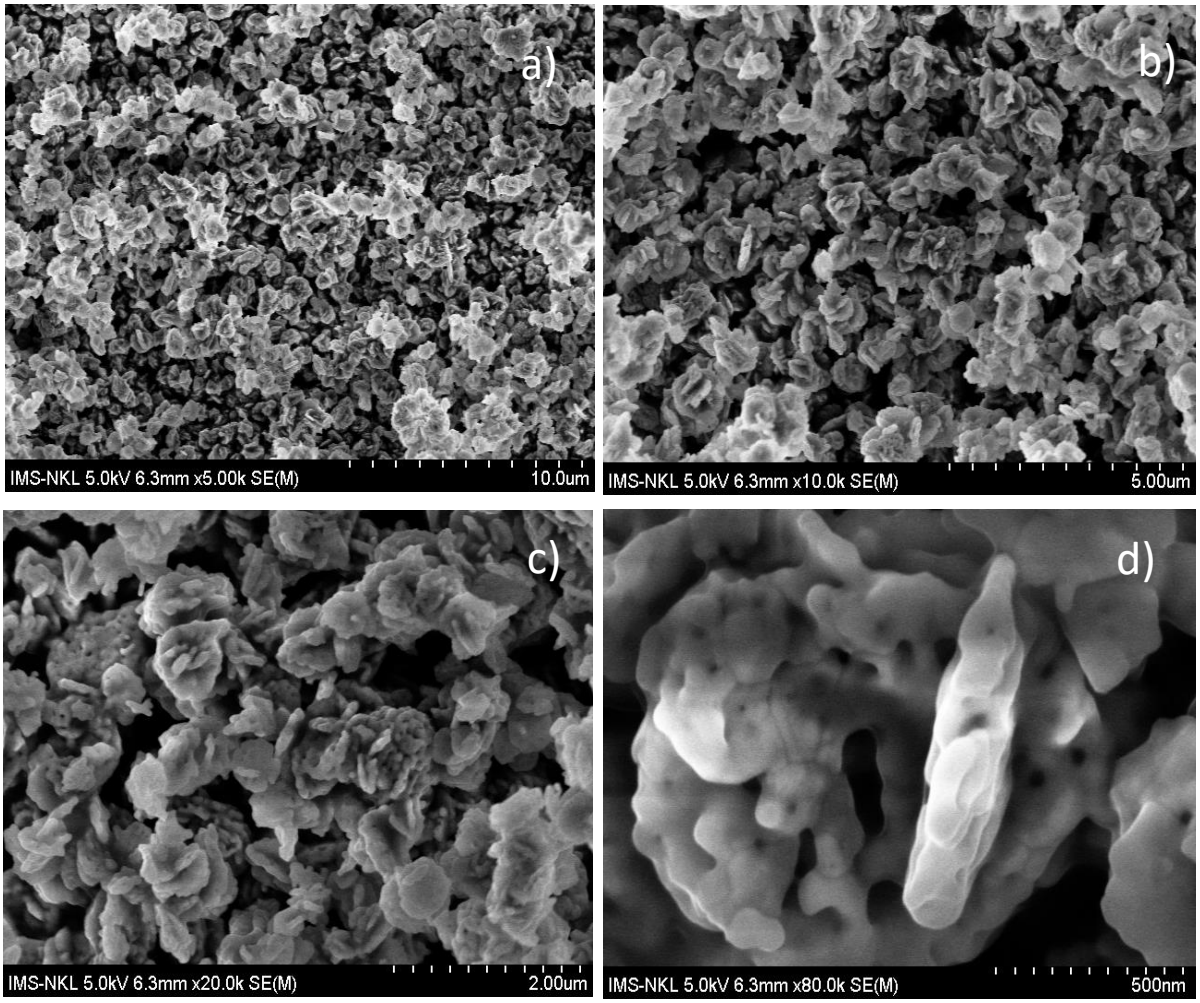

Figure 3.1. SEM images of $FePO_4$ sample

Figure 3.1 shows the SEM images of synthesized $FePO_4$ material with different magnification. It can be seen from the figure, $FePO_4$ form uniform particle, with the particle range in micrometer. For the carbon coated sample, which is shown in figure 3.2, there are brighter sites on the surface of the particle. It indicated the formation of carbon layer on the surface of LFP sample. It can be observed from Figure 3.2, the particle size of LFP/C-G20 sample is smaller than $FePO_4$ sample, which shows that the carbon coating contributes to the reduce in particle size. It prohibits the particle growth of the material through calcination. Smaller particle size can shorten the Li^+ diffusion path, therefore enhancing the electrochemical performance of the battery.

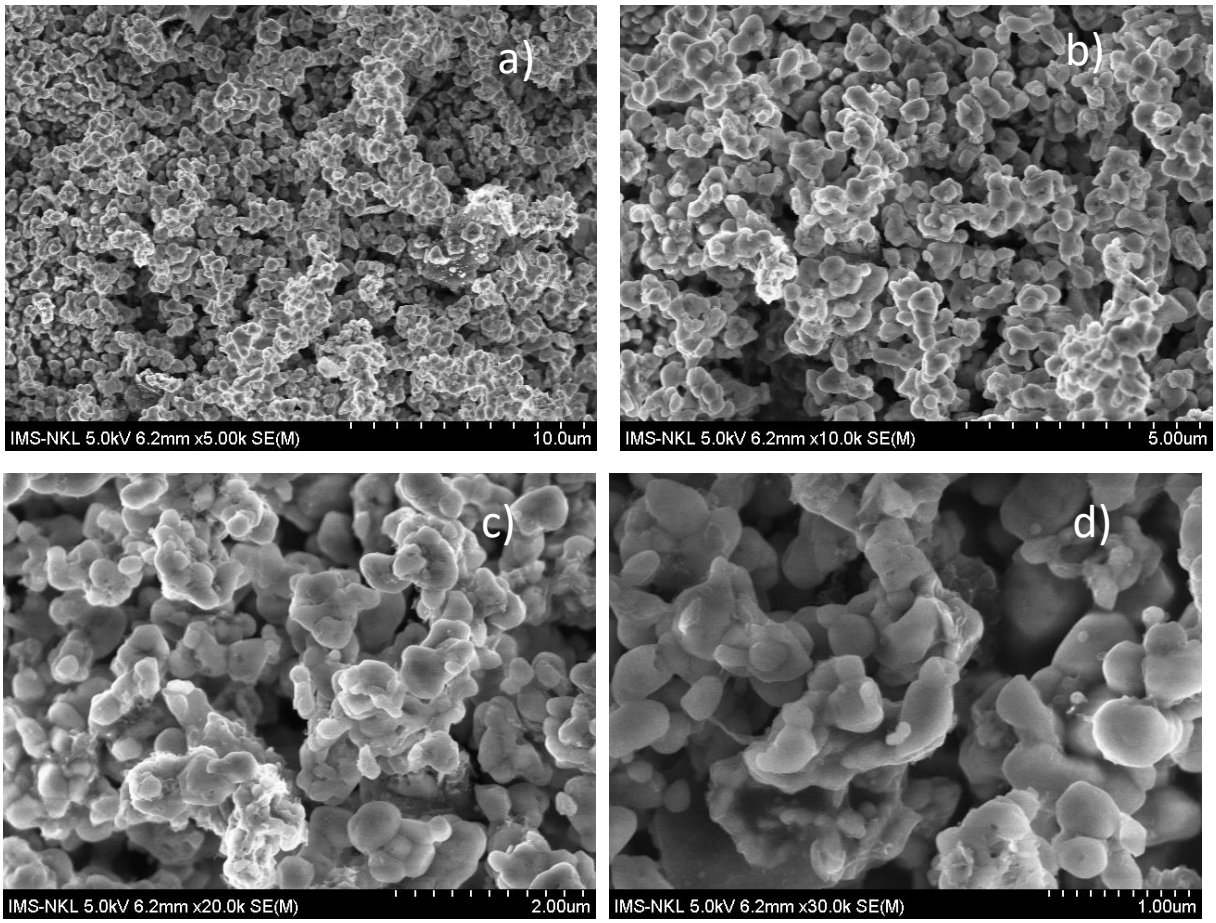

Figure 3.2. SEM images of LFP/C-G20

3.1.2. XRD patterns of $FePO_4$ and LFP/C samples

XRD analysis was used to investigate the evolution of phase during the synthesis. Figure 3.3a shows the XRD pattern of sample before calcination at 550 ℃ at 5 hours. The monoclinic $FePO_4.2H_2O$ was obtained, but the crystallinity was quite low. After calcination, the XRD pattern shows the formation of hexagonal $FePO_4$ (Figure 3.3b). The peaks achieve the same consistence to the standard peak of $FePO_4$ compound, which means the water had been removed after the dehydration.

For the XRD pattern of LFP/C-G20 (Figure 3.3c), the sample shows the single olivine-type phase, orthorhombic structure and no sencondary hased were obsreved. The peaks of carbons can not be seen because it has armophous structure, and also it had lower content than $LiFePO_4$, therefore their appearance does not affect the crystal structure.

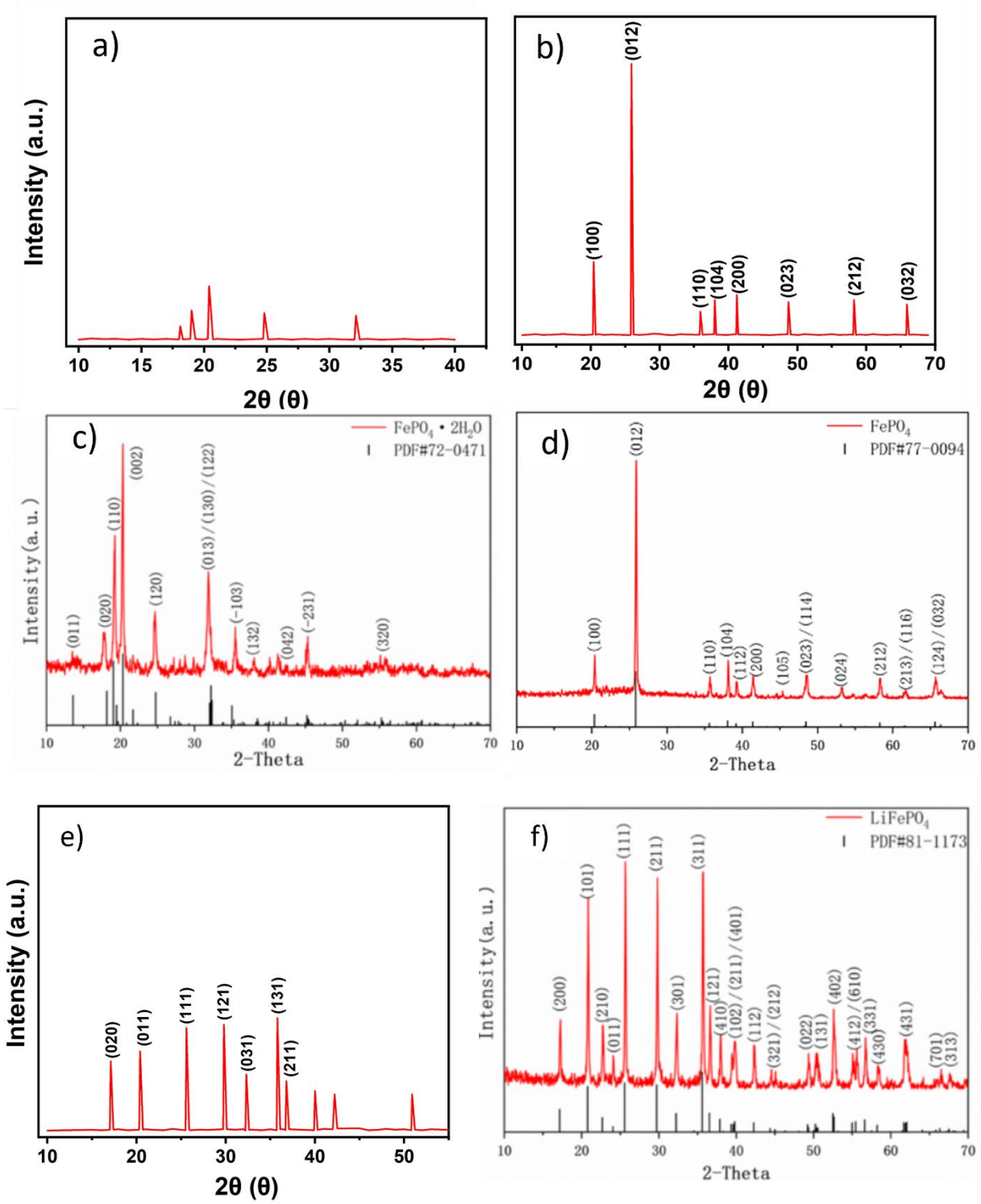

Figure 3.3. XRD patterns of a) $FePO_4.2H_2O$, b) $FePO_4$, e) $LiFePO_4$/C-G20 and standard peak of c) $FePO_4.2H_2O$, d) $FePO_4$, f) $LiFePO_4$ [58]

As repoted in some previous paper, some peaks of the impurities, for example, Fe_2P, Li_3PO_4, Fe_2O_3 could be appear because of the temperature or reducing agent [53]. However, there was no presence of the impurities due to the sintering at 700 ℃ and the controlling Ar atmosphere. At the temperature above 500 ℃, large amount of Fe^{3+} were

reduced to Fe^{2+}. Therefore, temperature 700 ℃ was the optimal sintering condition for the synthesis of LFP/C samples.

3.2. Influence of carbon coating in electrochemical performances of LFP

3.2.1. Charge-discharge curves of LFP/C samples

Figure 3.4a demonstrates the charge-discharge curves of LFP/C-G20 samples synthesized from different precursors: $FePO_4.2H_2O$ and $FePO_4$ at 0.1 C rate, potential range from 2.8 V to 3.8 V. It can be seen from the figure, LFP/C-G20 sample synthesized from $FePO_4$ has higher discharge capacity (117.12 mAh/g) compared to the sample synthesized from $FePO_4.H_2O$ (79.52 mAh/g). It is due to the poor crystallinity of $FePO_4.2H_2O$ sample.

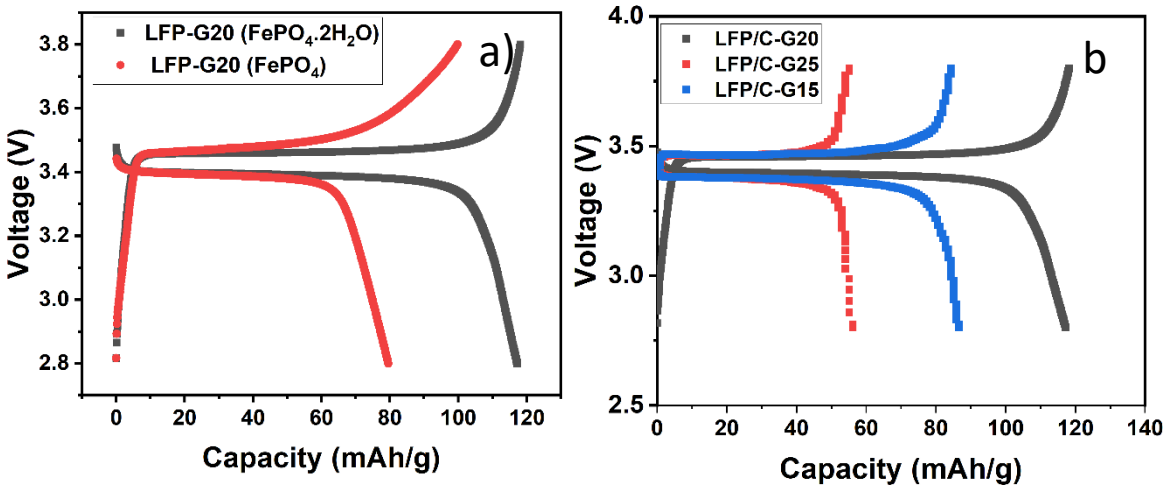

Figure 3.4. Charge-discharge curves of a) LFP/C-G20 synthesized from different precursors: $FePO_4.2H_2O$ and $FePO_4$, b) LFP/C with different glucose contents at 0.1C rate, potential range from 2.8 V to 3.8 V

Table 3.1: Carbon contents of LFP/C samples

Sample	Glucose content (%)	Carbon content (%)
LFP/C–G15	15	2.90
LFP/C–G20	20	5.22
LFP/C–G25	25	7.70

Figure 3.4b shows the charge-discharge curves of LFP/C samples with different glucose contents (15%, 20%, 25%, respectively). In 3 samples, LFP/C-G20 sample

exhibited the highest discharge capacity (117.12 mAh/g), and LFP/C-G25 obtained the lowest discharge capacity (55.18 mAh/g). Table 3.1 shows the theoretical calculation of carbon contents coated in each sample. The carbon content increased with the increase of glucose content. LFP/C-G20 sample can be considered to have more uniform coating layer compared to other sample, resulting in better electrochemical performance [54]. In contrast, too thick carbon coating in LFP/C-G25 sample lead to poor charge-discharge capacity, because it slows down the diffusion rate of Li^+ and the movement of Li^+ through thick carbon layered is also difficult [55]. Therefore, 20% mass content of glucose is the optimal amount for LFP/C synthesis.

3.2.2. Cyclic votammetry (CV) measurement of LFP/C samples

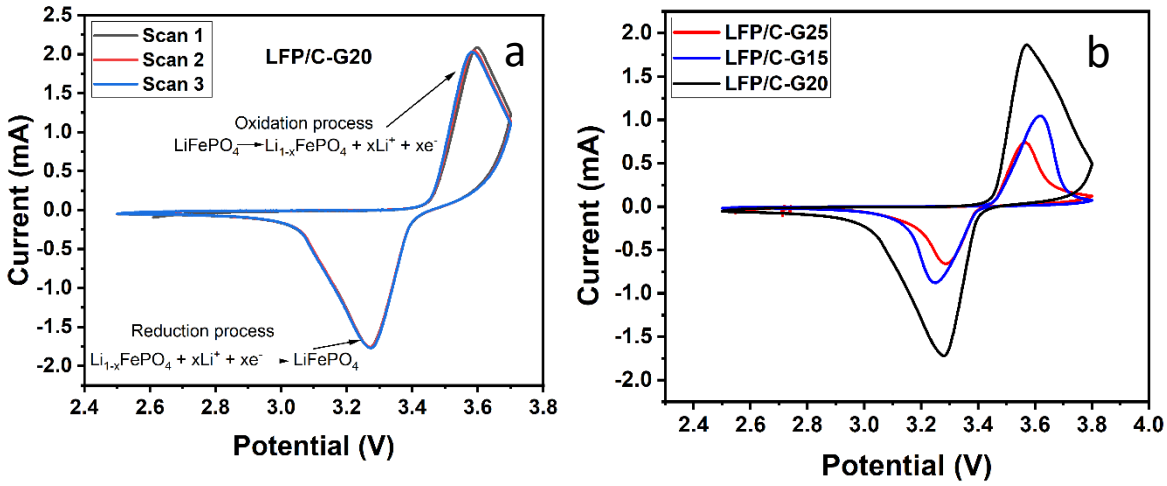

Figure 3.5. CVs graph of a) LFP/C-G20 sample in 3 scans and b) LFP/C-G15, G20, G25, potential range from 2.5 V to 3.8 V, scan rate 0.1mV s^{-1}

Figure 3.5b shows the cyclic voltammograms of 3 samples at the scan rate 0.1mV s^{-1} potential range from 2.5 V to 3.8 V. The potential of oxidation peaks are 3.59, 3.64, and 3.56 V, reduction process occurs at the potential 3.27, 3.24, and 3.28 V for LFP/C-G20, LFP/C-G15, LFP/C-G25 respectively. LFP–G20 exhibits more sharp peak and higher current signal compared to other sample which indicates that uniform carbon layer can enhance the diffusion of Li^+ ion and give high reversibility [56]. LFP/C-G25 sample shows the decrease in current signal, indicating that the cycle life of the cell is affected by thick coating. LFP-G20 also shows excellent stability after 3 scans (Figure 3.5a), with slightly change in the position of the oxidation and reduction peaks.

3.2.3. Electrochemical impedance spectrocopy measurement of the samples

To investigate the influence of coated carbon layer to the kinetics of the electrode, electrochemical impedance spectrocopy (EIS) of the 3 samples was measured with the frequency range from 0.1 Hz to 1 MHz, voltage aplitude ±10 mV. EIS graphs of 3 samples are shown by Figure 3.6. EIS measurment data is presented by Nyquist plots, with the semicircle ranging from high to medium frequency and inclined line belongs to the region of low frequency.

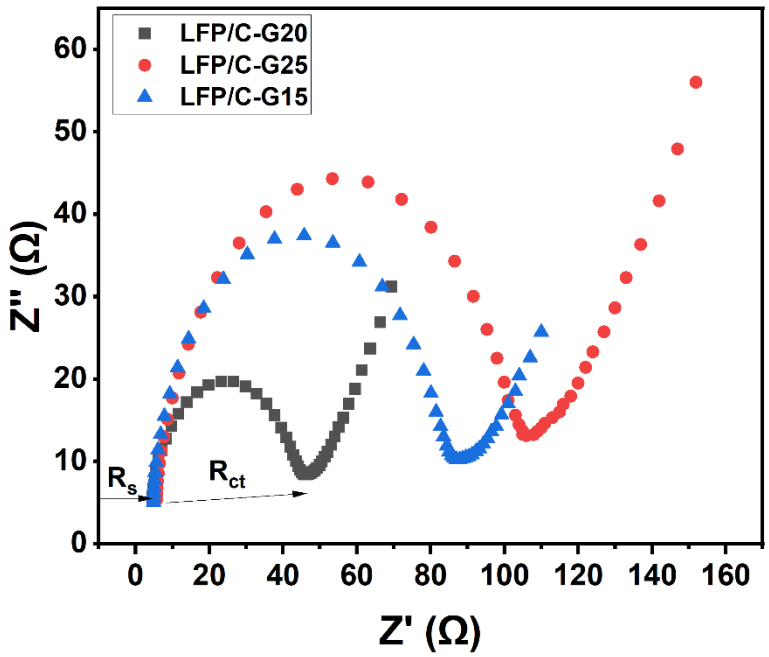

Figure 3.6. EIS graph of LFP/C samples

Different regions of the impedance spectrum reveal distinct electrical behaviors. At high frequencies, the intercept on the real axis indicates the ohmic resistance (R_S), which reflects the overall resistance of the electrolyte, separator, and current collector assembly. Moving to the medium frequencies, a depressed semicircle signifies the charge transfer resistance (R_{ct}) at the interface between the particles and the electrolyte. At low frequencies, an inclined line represents the Warburg impedance, associated with the diffusion of lithium ions within the $LiFePO_4$ particles.

Table 3.2. R_s and R_{ct} values of the LFP/C samples

	LFP/C–G15	LFP/C–G20	LFP/C–G25
R_s (Ω)	3.81	4.75	4.99
R_{ct} (Ω)	78.44	36.89	96.36

Table 3.2 shows the R_s and R_{ct} values of 3 samples. LFP–G20 sample has the lowest R_{ct} value because of the optimum carbon coating layer, providing conducting way for electron and Li+ ion diffusion, and decreasing the polarization [57]. For thick carbon coating of LFP/C-G25 sample, R_{ct} rises, this will decrease the Li^+ diffusion rate from and to LFP [56].

3.2.4. Influence of C-rates to charge-discharge capacity and cycling performace of LFP/C cathode material

3.2.4.1. Influence of C-rates to charge-discharge capacities

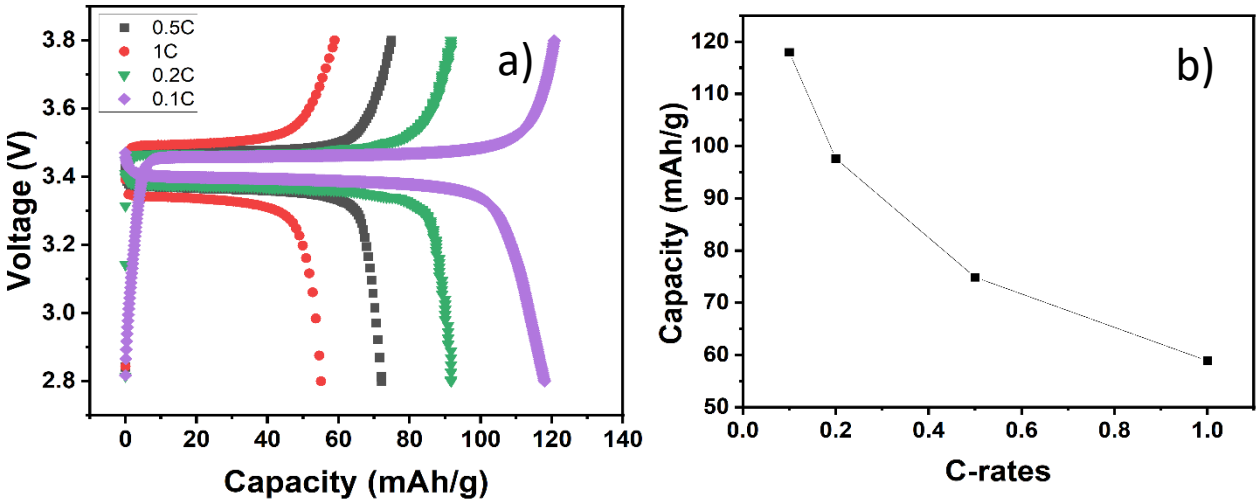

Figure 3.7. a) Charge-discharge curve of LFP-G20 sample with C-rates of 0.1C, 0.2C, 0.5C, 1C and b) Capacity vs C-rates.

The capacity of LFP/C-G20 sample was measure with different charge-discharge rates (0.1C, 0.2C, 0.5C, 1C). As can be seen from Figure 3.7a, with the increase of the C-rates, the distance between charge and discharge curve is bigger, indicatie the increase in resistance of the cell, leading to the drop of specific capacity. LFP/C-G20 sample obtain the capacity of 117.95 mAh/g at 0.1C, and 58.87 mAh/g at 1C.

3.2.4.1. Cyclic performance of LFP/C sample

Figure 3.8 shows the capacity retention of LFP/C-G20 sample after 64 cycles at 2C rates. The charge-discharge efficiency was remain 98% and the discharge retention was 95% after 64 cycles. This indicates that the carbon coating will provide not only good capacity but also enhance the cycle life of the battery, because it gives small polarization, fast electron and Li^+ ion transfer.

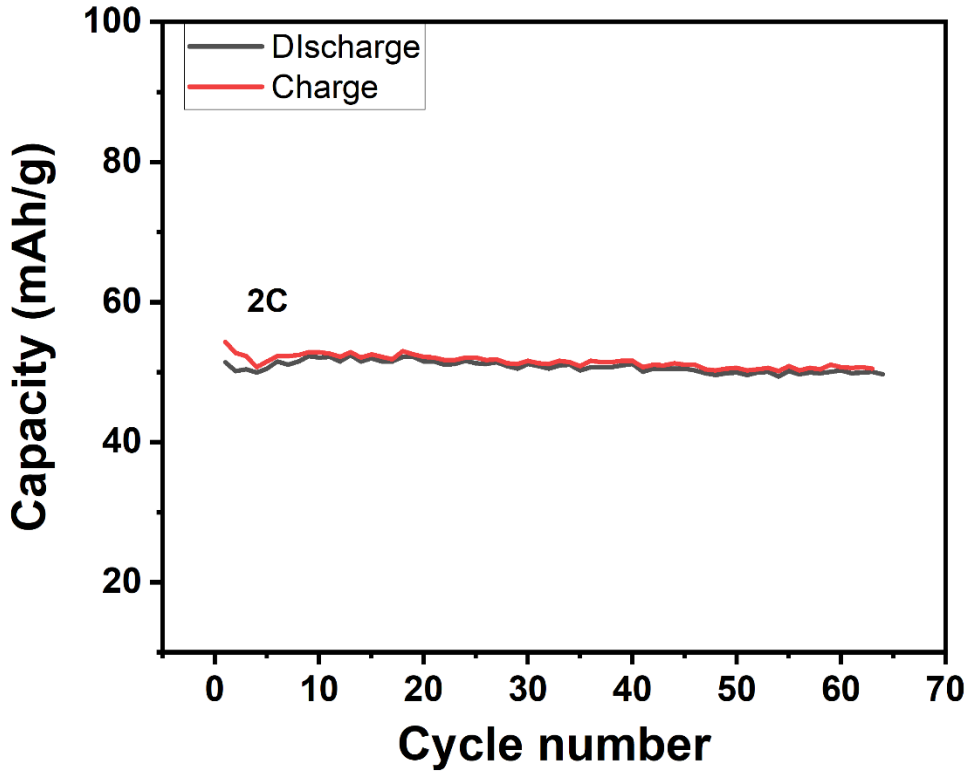

Figure 3.8. Cyclic performance pf LFP/C–G20 sample after 64 cycles, at 2C rate

CONCLUSION

In this research, $FePO_4$ and $LiFePO_4/C$ have been successfully synthesized using two processes: co-precipitation and calcination at high temperatures. The impact of varying glucose content, which acts as both a reducing agent and a carbon source, was investigated. Different techniques, including charge-discharge measurement, cyclic voltammetry (CV), and electrochemical impedance spectroscopy (EIS), were employed to analyze the electrochemical properties of the samples. The sample with a 5.22% mass content of carbon exhibited the best results, with a discharge capacity of 117.95 mAh/g, 95% capacity retention after 64 cycles at 2C, and low polarization and electron transfer resistance.

REFERENCES

1. Nitta, N., Wu, F., Lee, J. T., & Yushin, G. (2015). Li-ion battery materials: present and future. *Materials today*, *18*(5), 252-264.
2. Deng, D. (2015). Li-ion batteries: basics, progress, and challenges. *Energy Science & Engineering*, *3*(5), 385-418.
3. Deng, D., Kim, M. G., Lee, J. Y., & Cho, J. (2009). Green energy storage materials: Nanostructured TiO 2 and Sn-based anodes for lithium-ion batteries. *Energy & Environmental Science*, *2*(8), 818-837.
4. Kang, B., & Ceder, G. (2009). Battery materials for ultrafast charging and discharging. *Nature*, *458*(7235), 190-193.
5. Balakrishnan, P. G., Ramesh, R., & Kumar, T. P. (2006). Safety mechanisms in lithium-ion batteries. *Journal of power sources*, *155*(2), 401-414.
6. Megahed, S., & Scrosati, B. (1994). Lithium-ion rechargeable batteries. *Journal of Power Sources*, *51*(1-2), 79-104.
7. Fang, C., Deng, Y., Xie, Y., Su, J., & Chen, G. (2015). Improving the electrochemical performance of Si nanoparticle anode material by synergistic strategies of polydopamine and graphene oxide coatings. *The Journal of Physical Chemistry C*, *119*(4), 1720-1728.
8. Reddy, M. V., Subba Rao, G. V., & Chowdari, B. V. R. (2013). Metal oxides and oxysalts as anode materials for Li ion batteries. *Chemical reviews*, *113*(7), 5364-5457.
9. Wang, H., & Dai, H. (2013). Strongly coupled inorganic–nano-carbon hybrid materials for energy storage. *Chemical Society Reviews*, *42*(7), 3088-3113.
10. Murdock, B. E., Toghill, K. E., & Tapia-Ruiz, N. (2021). A perspective on the sustainability of cathode materials used in lithium-ion batteries. *Advanced Energy Materials*, *11*(39), 2102028.
11. Chung, S. Y., Bloking, J. T., & Chiang, Y. M. (2002). Electronically conductive phospho-olivines as lithium storage electrodes. *Nature materials*, *1*(2), 123-128.
12. Maleki, H., Deng, G., Kerzhner-Haller, I., Anani, A., & Howard, J. N. (2000). Thermal stability studies of binder materials in anodes for lithium-ion batteries. *Journal of the Electrochemical Society*, *147*(12), 4470.
13. Shim, J., Kostecki, R., Richardson, T., Song, X., & Striebel, K. A. (2002). Electrochemical analysis for cycle performance and capacity fading of a lithium-ion battery cycled at elevated temperature. *Journal of power sources*, *112*(1), 222-230.
14. Mazouzi, D., Lestriez, B., Roué, L., & Guyomard, D. (2009). Silicon composite electrode with high capacity and long cycle life. *Electrochemical and Solid-State Letters*, *12*(11), A215.
15. Huang, X. (2011). Separator technologies for lithium-ion batteries. *Journal of Solid State Electrochemistry*, *15*(4), 649-662.
16. Zhang, W. J. (2011). Structure and performance of LiFePO4 cathode materials: A review. *Journal of Power Sources*, *196*(6), 2962-2970.

17. Tarascon, J. M., & Armand, M. (2001). Issues and challenges facing rechargeable lithium batteries. *nature*, *414*(6861), 359-367.
18. Padhi, A. K., Nanjundaswamy, K. S., & Goodenough, J. B. (1997). Phospho-olivines as positive-electrode materials for rechargeable lithium batteries. *Journal of the electrochemical society*, *144*(4), 1188.
19. Kim, D. H., & Kim, J. (2006). Synthesis of LiFePO4 nanoparticles in polyol medium and their electrochemical properties. *Electrochemical and Solid-State Letters*, *9*(9), A439.
20. Yamada, A., Hosoya, M., Chung, S. C., Kudo, Y., Hinokuma, K., Liu, K. Y., & Nishi, Y. (2003). Olivine-type cathodes: Achievements and problems. *Journal of Power Sources*, *119*, 232-238.
21. Hannoyer, B., Prince, A. A. M., Jean, M., Liu, R. S., & Wang, G. X. (2007). Mössbauer study on LiFePO 4 cathode material for lithium ion batteries. In *ICAME 2005: Proceedings of the 28th International Conference on the Applications of the Mössbauer Effect (ICAME 2005) held in Montpellier, France, 4–9 September 2005 Volume II (Part III–V/V)* (pp. 767-772). Springer Berlin Heidelberg.
22. Yada, C., Iriyama, Y., Jeong, S. K., Abe, T., Inaba, M., & Ogumi, Z. (2005). Electrochemical properties of LiFePO4 thin films prepared by pulsed laser deposition. *Journal of power sources*, *146*(1-2), 559-564.
23. Nakamura, T., Miwa, Y., Tabuchi, M., & Yamada, Y. (2006). Structural and surface modifications of LiFePO4 olivine particles and their electrochemical properties. *Journal of the Electrochemical Society*, *153*(6), A1108.
24. Yang, M. R., Teng, T. H., & Wu, S. H. (2006). LiFePO4/carbon cathode materials prepared by ultrasonic spray pyrolysis. *Journal of power Sources*, *159*(1), 307-311.
25. Xia, H., Lu, L., & Ceder, G. (2006). Li diffusion in LiCoO2 thin films prepared by pulsed laser deposition. *Journal of Power Sources*, *159*(2), 1422-1427.
26. Dathar, G. K. P., Sheppard, D., Stevenson, K. J., & Henkelman, G. (2011). Calculations of Li-ion diffusion in olivine phosphates. *Chemistry of Materials*, *23*(17), 4032-4037.
27. Islam, M. S., Driscoll, D. J., Fisher, C. A., & Slater, P. R. (2005). Atomic-scale investigation of defects, dopants, and lithium transport in the LiFePO4 olivine-type battery material. *Chemistry of Materials*, *17*(20), 5085-5092.
28. Kuenzel, M., Porhiel, R., Bresser, D., Asenbauer, J., Axmann, P., Wohlfahrt-Mehrens, M., & Passerini, S. (2020). Deriving structure-performance relations of chemically modified chitosan binders for sustainable high-voltage LiNi0. 5Mn1. 5O4 cathodes. *Batteries & Supercaps*, *3*(2), 155-164.
29. Ning, F., Li, S., Xu, B., & Ouyang, C. (2014). Strain tuned Li diffusion in LiCoO2 material for Li ion batteries: A first principles study. *Solid State Ionics*, *263*, 46-48.
30. Wang, J., & Sun, X. (2012). Understanding and recent development of carbon coating on LiFePO 4 cathode materials for lithium-ion batteries. *Energy & Environmental Science*, *5*(1), 5163-5185.

31. Fang, H., Pan, Z., Li, L., Yang, Y., Yan, G., Li, G., & Wei, S. (2008). The possibility of manganese disorder in LiMnPO4 and its effect on the electrochemical activity. *Electrochemistry communications*, *10*(7), 1071-1073.
32. Toprakci, O., Toprakci, H. A., Ji, L., & Zhang, X. (2010). Fabrication and electrochemical characteristics of LiFePO4 powders for lithium-ion batteries. *KONA Powder and Particle Journal*, *28*, 50-73.
33. Yang, Z., Dai, Y., Wang, S., & Yu, J. (2016). How to make lithium iron phosphate better: a review exploring classical modification approaches in-depth and proposing future optimization methods. *Journal of materials chemistry A*, *4*(47), 18210-18222..
34. Srinivasan, V., & Newman, J. (2004). Discharge model for the lithium iron-phosphate electrode. *Journal of the Electrochemical Society*, *151*(10), A1517.
35. Andersson, A. S., & Thomas, J. O. (2001). The source of first-cycle capacity loss in LiFePO4. *Journal of Power Sources*, *97*, 498-502.
36. Laffont, L., Delacourt, C., Gibot, P., Wu, M. Y., Kooyman, P., Masquelier, C., & Tarascon, J. M. (2006). Study of the LiFePO4/FePO4 two-phase system by high-resolution electron energy loss spectroscopy. *Chemistry of materials*, *18*(23), 5520-5529.
37. Delmas, C., Maccario, M., Croguennec, L., Le Cras, F., & Weill, F. (2008). Lithium deintercalation in LiFePO4 nanoparticles via a domino-cascade model. *Nature materials*, *7*(8), 665-671.
38. Pei, B., Yao, H., Zhang, W., & Yang, Z. (2012). Hydrothermal synthesis of morphology-controlled LiFePO4 cathode material for lithium-ion batteries. *Journal of Power Sources*, *220*, 317-323.
39. Yu, F., Zhang, J., Yang, Y., & Song, G. (2010). Porous micro-spherical aggregates of LiFePO4/C nanocomposites: A novel and simple template-free concept and synthesis via sol–gel-spray drying method. *Journal of Power Sources*, *195*(19), 6873-6878.
40. Xie, G., Zhu, H. J., Liu, X. M., & Yang, H. (2013). A core–shell LiFePO4/C nanocomposite prepared via a sol–gel method assisted by citric acid. *Journal of alloys and compounds*, *574*, 155-160.
41. Ding, Y., Jiang, Y., Xu, F., Yin, J., Ren, H., Zhuo, Q., ... & Zhang, P. (2010). Preparation of nano-structured LiFePO4/graphene composites by co-precipitation method. *Electrochemistry Communications*, *12*(1), 10-13.
42. Zhu, Y., Tang, S., Shi, H., & Hu, H. (2014). Synthesis of FePO4· xH2O for fabricating submicrometer structured LiFePO4/C by a co-precipitation method. *Ceramics International*, *40*(2), 2685-2690.
43. Ahsan, Z., Ding, B., Cai, Z., Wen, C., Yang, W., Ma, Y., ... & Javed, M. S. (2021). Recent progress in capacity enhancement of LiFePO4 cathode for Li-ion batteries. *Journal of Electrochemical Energy Conversion and Storage*, *18*(1), 010801.
44. Kulka, A., Walczak, K., Zając, W., & Molenda, J. (2017). Effect of reducing agents on low-temperature synthesis of nanostructured LiFePO4. *Journal of Solid State Chemistry*, *253*, 367-374.

45. Su, J., Wu, X. L., Yang, C. P., Lee, J. S., Kim, J., & Guo, Y. G. (2012). Self-assembled LiFePO4/C nano/microspheres by using phytic acid as phosphorus source. *The Journal of Physical Chemistry C*, *116*(8), 5019-5024.
46. Chen, M., Wang, X., Shu, H., Yu, R., Yang, X., & Huang, W. (2015). Solvothermal synthesis of monodisperse micro-nanostructure starfish-like porous LiFePO4 as cathode material for lithium-ion batteries. *Journal of Alloys and Compounds*, *652*, 213-219.
47. Ma, Z., Shao, G., Fan, Y., Wang, G., Song, J., & Liu, T. (2014). Tunable morphology synthesis of LiFePO4 nanoparticles as cathode materials for lithium ion batteries. *ACS Applied Materials & Interfaces*, *6*(12), 9236-9244.
48. Zhang, Y., Huo, Q. Y., Du, P. P., Wang, L. Z., Zhang, A. Q., Song, Y. H., ... & Li, G. Y. (2012). Advances in new cathode material LiFePO4 for lithium-ion batteries. *Synthetic Metals*, *162*(13-14), 1315-1326.
49. Jugović, D., & Uskoković, D. (2009). A review of recent developments in the synthesis procedures of lithium iron phosphate powders. *Journal of Power Sources*, *190*(2), 538-544.
50. Liu, H., Li, C., Zhang, H. P., Fu, L. J., Wu, Y. P., & Wu, H. Q. (2006). Kinetic study on LiFePO4/C nanocomposites synthesized by solid state technique. *Journal of Power Sources*, *159*(1), 717-720.
51. Rao, Y., Wang, K., & Zeng, H. (2015). The effect of phenol–formaldehyde resin on the electrochemical properties of carbon-coated LiFePO4 materials in pilot scale. *Ionics*, *21*(6), 1525-1531.
52. Cheng, Q., Zhao, X., Yang, G., Mao, L., Liao, F., Chen, L., ... & Chen, S. (2021). Recent advances of metal phosphates-based electrodes for high-performance metal ion batteries. *Energy Storage Materials*, *41*, 842-882.
53. Dou, J., Kang, X., Wumaier, T., Hua, N., Han, Y., & Xu, G. (2012). Oxalic acid-assisted preparation of LiFePO 4/C cathode material for lithium-ion batteries. *Journal of Solid State Electrochemistry*, *16*, 1925-1931.
54. Chang, Y. C., Peng, C. T., & Hung, I. M. (2014). Effects of particle size and carbon coating on electrochemical properties of LiFePO 4/C prepared by hydrothermal method. *Journal of Materials Science*, *49*, 6907-6916.
55. Cho, Y. D., Fey, G. T. K., & Kao, H. M. (2009). The effect of carbon coating thickness on the capacity of LiFePO4/C composite cathodes. *Journal of Power Sources*, *189*(1), 256-262.
56. Liu, H., & Tang, D. (2008). The low cost synthesis of nanoparticles LiFePO4/C composite for lithium rechargeable batteries. *Solid State Ionics*, *179*(33-34), 1897-1901.
57. Shin, H. C., Cho, W. I., & Jang, H. (2006). Electrochemical properties of the carbon-coated LiFePO4 as a cathode material for lithium-ion secondary batteries. *Journal of Power Sources*, *159*(2), 1383-1388.
58. Dong, J., He, H., He, Q., Zhang, D., & Chang, C. (2019). Cost effective and eco-friendly synthesis of LiFePO 4/C cathode material from a natural mineral magnetite. *Journal of Materials Science: Materials in Electronics*, *30*, 17128-17136.